SAND2011-1921C

A bond-order potential based molecular dynamics method for CdTe vapor deposition simulations

X. W. Zhou[1], D. Ward[2], B. M. Wong[3], F. P. Doty[2], J. A. Zimmerman[1], G. N. Nielson[4], J. L. Cruz-Campa[4], J. E. Granata[5], and D. Zubia[6]

[1] *Mechanics of Materials Department, Sandia National Laboratories, Livermore, CA 94550, USA*

[2] *Rad/Nuc Detection Materials and Analysis Department, Sandia National Laboratories, Livermore, CA 94550, USA*

[3] *Materials Chemistry Department, Sandia National Laboratories, Livermore, CA 94550, USA*

[4] *Advanced MEMS Department, Sandia National Laboratories, Albuquerque, NM 87185, USA*

[5] *Photovoltaics and Grid Integration Department, Sandia National Laboratories, Albuquerque, NM 87185, USA*

[6] *Department of Electrical Engineering, University of Texas at El Paso, El Paso, TX 79968, USA*

ABSTRACT

CdTe has been a special semiconductor for constructing the lowest-cost solar cells and the CdTe-based $Cd_{1-x}Zn_xTe$ alloy has also been the leading semiconductor for radiation detection applications. The performance currently achieved for the materials, however, is still far below the theoretical expectations. This is because the property-limiting nanoscale defects that are easily formed during the growth of CdTe crystals are difficult to explore in experiments. Here we demonstrate the capability of the currently state-of-the-art bond order potential-based molecular dynamics method in the prediction of the crystalline growth of CdTe films during vapor

deposition simulations. Such a method may begin to enable defects generated during vapor deposition of CdTe crystals to be explored in high fidelity atomistic simulations.

Keywords: CdTe, $Cd_{1-x}Zn_xTe$, CZT, bond-order potential, molecular dynamics, vapor deposition

I. INTRODUCTION

The CdTe semiconductor compound is attractive for two important applications. In one application, CdTe films are used to produce terrestrial solar cells [1,2] at a production cost lower than any other photovoltaic technologies [3,4] currently available. This is because the material has good manufacturability, high solar energy absorption coefficient, and optimal band gap for photoelectric conversion under solar radiation [5,6,7]. In the other application, the CdTe-based $Cd_{1-x}Zn_xTe$ (CZT) alloys have been the dominant semiconductors for radiation detections [8,9,10,11]. This is because these alloys have high atomic numbers for efficient radiation-atomic interactions, and ideal band gaps for both a high electron-hole creation and a low leakage current. Despite of the successful application of CdTe and CZT, the potential for material improvement is still tremendous. For instance, the record energy conversion efficiency currently achieved for the CdTe solar cells is only about 16% as compared with the theoretical prediction of 29% [5,12,13,14]. The difference has been related to various micro / nano scale defects in the multilayered films [7,4,12,15,16,17]. The property nonuniformity of the radiation detecting CZT crystals, on the other hand, has been the limiting factor for both a poor performance and a high material cost (arising from a low yield of usable portion of ingots) [8]. Grain boundaries and tellurium inclusions / precipitates are known to cause carrier transport nonuniformity [8,18,19]. Native defects such as vacancies, antisites, and interstitials can also affect properties [20,21]. The

problem is that these defects are difficult to remove especially because their formation mechanisms are not clearly understood currently. Note that some defects, such as dislocations [22], are prevalent in the materials but have not been well studied in the past. Clearly a high fidelity modeling approach that can reveal the formation of various defects as a function of processing conditions and ways to control them during growth can guide the growth optimization, likely leading to further material improvement. This in turn impacts a wide range of applications including national security, medical imaging, environmental safety and remediation, and industrial processing monitoring.

Molecular dynamics (MD) simulations solve the positions of atoms as a function of time using the fundamental Newton's equation of motion and therefore can track the defect evolution at an atomic scale resolution. The key to high fidelity molecular dynamics simulations of CdTe crystal growth is the use of an accurate interatomic potential that is transferrable to a variety of configurations. The objective of the present work is twofold: (a) identify the current state-of-the-art interatomic potential for CdTe and demonstrate its capability in the vapor deposition simulations of CdTe thin film growth; and (b) by carrying out extensive vapor deposition simulations, establish qualitatively correlations between film quality (say, crystallinity, stoichiometry, and various antisite concentrations) and deposition conditions (mainly substrate temperature and vapor phase species ratio).

II. SIMULATION METHODS

A. Interatomic potential

Our study indicated that there are two CdTe interatomic potentials available in the literature, one [23] is parameterized using the Stillinger-Weber potential format (SW) [27], and the other one [24] is parameterized using a Rockett modification [25] of the Tersoff potential format (TR)

[28]. Recently we also developed a CdTe bond order potential (BOP) [26]. Unlike the Stillinger-Weber [27] and Tersoff/Brenner [28,29] types of potentials commonly used for semiconductor systems in the past, a special feature of this BOP is that it is strictly derived from quantum mechanics theory [30,31,32,33,34,35] and therefore can be more transferrable if well parameterized. For this particular CdTe BOP [26], parameterization was performed considering the structures and energies of a variety of clusters, lattices, and defects. Detailed description of the BOP formalism can be found in previous work [26,36]. BOP uses global-, species-, pair- and triple- parameters. These parameters for the parameterized CdTe BOP [26] are listed respectively in Tables I-IV.

Table I. Global BOP parameters for CdTe.

Symbol	Term	---
ς_4	small number in Eq. (9)	0.00001
ς_5	small number in Eq. (12)	0.00001
ς_6	small number in Eq. (16)	0.00100
ς_7	small number in Eq. (16)	0.00001

Table II. Species-dependent BOP parameters for CdTe.

Symbol	Term	Cd	Te
p_π	see Eq. (19)	0.420000	0.460686

Table III. Pair-dependent BOP parameters for CdTe.

Symbol	Term	Cd-Cd	Te-Te	Cd-Te
r_0	GSP reference radius (Å)	3.1276	3.1626	3.1276
r_c	GSP characteristic radius (Å)	3.1276	3.1626	3.1276
r_1	cutoff start radius (Å)	3.7303	3.8046	4.0138
r_{cut}	cutoff radius (Å)	4.3330	4.4465	4.9000
n_c	GSP decay exponent	2.800000	2.799998	2.811251
m	GSP attractive exponent	3.263155	2.458846	2.587831
n	GSP repulsive exponent	1.553883	1.223306	1.287478
ϕ_0	repulsive energy prefactor (eV)	0.186369	0.876912	0.631440
$\beta_{\sigma,0}$	σ bond integral prefactor (eV)	0.238318	0.782635	0.825290
$\beta_{\pi,0}$	π bond integral prefactor (eV)	0.097599	0.531205	0.031743
c_σ	empirical Θ_σ parameter	0.561130	1.014809	1.286955
f_σ	band-filling parameter	0.431863	0.331227	0.5
k_σ	skewing prefactor	15.00000	-2.86019	0

c_π	empirical Θ_π parameter	1	1	1
a_π	prefactor for Θ_π	1	1	1

Table IV. Three-body-dependent BOP parameters for CdTe

Symbol	Term	jik					
		CdCdCd	TeTeTe	TeCdTe	CdCdTe	CdTeCd	CdTeTe
p_σ	see Eq. (11)	1	1	1	1	1	1
b_σ	see Eq. (11)	0.762039	0.669623	0.200000	1.000000	0.2000000	0.999854
u_σ	see Eq. (11)	-0.40000	-0.14152	-0.38336	0.099711	-0.400000	-0.00393

Careful studies haves been performed to calculate a variety of properties using all the three potentials as well as density functional theory (DFT) [26,37]. As representative examples for comparing the fidelity of different models, some results are reproduced in Fig. 1 and Table V, which show respectively the cohesive energies of a variety of Cd, Te, and CdTe phases, and the energies of various defects in the equilibrium zinc-blende CdTe crystal. Here various lattices are abbreviated as diamond-cubic (dc), simple-cubic (sc), body-centered-cubic (bcc), face-centered-cubic (fcc), hexagonal-close-packed (hcp), graphite (gra), graphene (grap), γ-Se (A8), zinc-blende (zb), wurtzite (wz), B1 (NaCl), B2 (CsCl), and face-centered-plane (fcp). In Fig. 1, the experimental values of the cohesive energies [38] of the equilibrium phases are also shown using the unfilled circles, and the straight lines connecting the neighboring data points are used to guide eyes. Because the DFT calculations typically give accurate relative energies but not the absolute energies, the cohesive energies obtained from DFT calculations are scaled so that they match the experimental values for the equilibrium phases. Fig. 1 indicates that the cohesive energies calculated using the BOP model (the red lines) are considerably closer to those predicted by the DFT (the blue lines) than the corresponding results of the SW and TR parameterizations. Most importantly, Fig. 1(a) shows that the BOP correctly specify the lowest energies for the equilibrium phases for both elements and the compound, namely, the hcp Cd, the

A8 Te, and the zb CdTe, and the calculated cohesive energies of the lowest energy phases also match the corresponding experimental values. In sharp contrast, the lowest energy phases are calculated to be dc Cd, dc Te, and zb CdTe by the SW parameterization and dc Cd, bcc Te, and CsCl by the TR parameterization, where the only correct result is the zb CdTe structure by the SW parameterization. These results indicate that the TR parameterization cannot be used to study any of the equilibrium Cd, Te, and CdTe phases as the structures will not be even stable in MD simulations. While the SW parameterization can be used in some sort of MD simulations to study the equilibrium CdTe phase, caution should be taken in explaining the results concerning defects as the potential is not transferrable to Cd and Te (and hence the defective) regimes.

Table V. Defect energies of zinc-blende CdTe (eV)

defect type	DFT	BOP	SW	TR
Cd vacancy	2.20	2.66	2.60	2.43
Te vacancy	2.72	1.64	1.53	0.93
Cd antisite	3.01	3.24	0.80	0.18
Te antisite	3.16	2.04	0.74	1.19
Cd-in-Cd interstitial	1.98	1.21	4.27	1.36
Te-in-Cd interstitial	3.52	2.92	2.60	0.55
Cd-in-Te interstitial	2.14	2.12	3.76	0.61
Te-in Te interstitial	3.91	2.92	3.57	1.28

Table V indicates that the general trend of energies of various defects calculated using the BOP method is also much closer to that of the DFT calculations than the results from SW and TR parameterizations. In particular, SW parameterization indicates that Cd antisite and Te antisite have the lowest energies (0.74 – 0.80) eV and should be the dominant defects whereas the DFT calculations indicate very high energies (> 3.00 eV) for these two defects. Worse than that, the TR parameterization indicates an extremely low energy of 0.18 eV for the Cd antisite. Note that defect energies are calculated using the lowest energy elemental phases as the reference states [39,40,41]. The wrong values of defect energies are hence on top of the wrong

elemental structures. On the other hand, both BOP and DFT give the lowest energies for the Cd-in-Cd interstitial. It is for these reasons that the BOP can produce more accurate results than the other methods currently available in literature. Hence, we use the BOP [26] in the present work.

B. Molecular dynamics model

The BOP potential [26] has been implemented in a serial MD code. This allows us to perform MD simulations of CdTe vapor deposition at a relatively small scale. Nonetheless, it is sufficient for demonstrating the capability of the BOP-based MD method in vapor deposition simulations and establishing qualitatively the trend of deposited film quality as a function of deposition conditions. For vapor deposition simulations, an initial substrate of a zb crystal containing 215 Cd atoms and 216 Te atoms with 6 (101) layers in the x- direction, 12 (040) layers in the y- direction, and 6 ($\bar{1}01$) layers in the z- direction was first created using an initial lattice constant of a = 6.882 Å. The top y surface was terminated by Cd initially. Periodic boundary conditions were used in the x- and z- directions so that the system can be viewed as infinitely large in these two directions. A free boundary condition was used in the y- direction to enable deposition on the top (040) surface. During simulations, the bottom 3 (040) layers were fixed. A simulated growth temperature was created by assigning velocities to each of the remaining atoms based upon a Boltzmann probability distribution. The subsequent evolution of positions and velocities of system atoms was then solved from interatomic forces and Newton's equation of motion using Nordsieck's numerical integration algorithm [42]. A Lagrangian formalism that enables the periodic lengths to change during simulation [43] was adopted to relax stresses. To ensure a constant substrate temperature, all the other atoms above the fixed region were controlled using a Nose-Hoover isothermal algorithm [44]. Growth was simulated by injecting Cd and Te vapor species from random locations far above the surface. The injecting

frequencies of the two species were determined from the simulated deposition rate and Te:Cd vapor species ratio. The injected atoms were all assigned a remote incident kinetic energy. To capture the adatom incident energy effects, the newly added adatoms were not isothermally controlled until they were fully incorporated into the film and their initial kinetic and potential (latent heat release) energies were fully dissipated. Simulations were performed at various substrate temperatures T between 700 and 1200 K, adatom incident energies E_i between 0.1 and 1.0 eV, deposition rates R between 2 and 12 nm/ns, vapor species ratio Te:Cd between 0.8 and 1.5, two different tellurium vapor species of atomic Te and molecular Te_2 (cadmium vapor species was always in atomic Cd form), and a constant adatom incident angle $\theta = 0^o$ (i.e., the adatom initial impact direction was normal to the surface).

III. RESULTS

A. Deposition rate effects

The deposition rates used in MD simulations are orders of magnitude higher than those used in experiments due to the constraint of the computational cost. The main effects of accelerated deposition rates on film structures can be understood using a simple analysis. Consider that when adatoms are first condensed on a growth surface, they must quickly move to some close local minimum energy sites on the surface because the process is either associated with a small energy barrier or is barrierless. These local minimum energy sites are likely to be the lattice sites so that even these adatoms do not further move, they can still be buried by subsequently deposited atoms to result in a crystalline growth. This fast initial relaxation of adatoms to the nearby surface lattice sites can be captured by MD simulations at the accelerated deposition rates. Once occupy the surface lattice sites, the adatoms can undergo various diffusion processes to migrate to lower energy sites that may be a distance away, leading to the evolution of surface

morphology towards more stable configurations. The diffusion jumps of surface atoms from one lattice site to another must be thermally activated as they are associated with significant energy barriers, and hence are relatively slow. It can be seen that the net effects of the accelerated deposition rates used in MD simulations are to cause the surface atoms to be rapidly buried into the bulk so that their surface diffusion is significantly underestimated.

While the simulated deposition rates are much higher than those in reality, understanding film structure vs. deposition rate in the simulation regime is still important. First, there exists a substrate temperature dependent critical simulated deposition rate above which amorphous films are always obtained regardless of the interatomic potential. This occurs because the adatoms do not even have time and mobility to relax to the close lattice sites before being fully buried when the deposition rate exceeds the critical value. Understanding this critical deposition rate, therefore, is necessary to design meaningful simulations. Second, the underestimation of the surface diffusion by using accelerated deposition rates may be mitigated by using elevated substrate temperature that promotes the diffusion. Hence, the simulated structure vs. deposition rate relation may still qualitatively reflect the reality with the temperature acceleration scheme. Hence, we first examine the effect of deposition rate.

1. Atomic structure observation

Simulations were performed at a constant substrate temperature of 1200 K, a constant adatom energy of 0.1 eV, a constant Te:Cd vapor species ratio of 1, and various deposition rates between 2 and 14 nm/ns, using molecular tellurium vapor phase Te_2. The 0.1 eV adatom energy reflects well the thermal deposition processes commonly used to grow semiconductor films and the molecular tellurium vapor phase is also frequently used in experiments [] as this phase is relatively stable. Examples of the simulated CdTe films obtained at ~2.7, ~5.4, ~8.1, and ~11.2

nm/ns are shown respectively in Figs. 2(a) – 2(d). In Fig. 2, the parameters ξ, X, $f_{Cd@Te}$ and $f_{Te@Cd}$ represent respectively the crystallinity, the stoichiometry parameter, and the Cd@Te and Te@Cd antisites concentrations. These parameters will be described in more details below, but for reference, $\xi = 1$, $X = 1$, $f_{Cd@Te} = 0$, and $f_{Te@Cd} = 0$ would correspond to an ideal zb CdTe crystal at 0 K. It can be from Fig. 2(d) that at a high deposition rate of ~ 11 nm/ns, the atomic structure near the surface region is amorphous, and a portion of the film below the surface appears to be a metastable lattice different from the zb CdTe. Not surprisingly, Fig. 2(d) is accompanied by a low crystallinity parameter and high antisites defect concentrations as compared to Figs. 2(a)-2(c). The poor structure indicated that the high deposition rate of 11.2 nm/ns is likely to be above the critical deposition rate discussed above so that adatoms did not have sufficient time to relax to the nearby zb lattice sites before being buried by the new adatoms. In the particular case shown in Fig. 2(d), this would trigger the formation of a metastable crystal structure, which could not sustain due to the same reason, eventually leading to the formation of amorphous structure.

When the deposition rate was reduced to ~ 8 nm/ns, Fig. 2(c), adatoms had more time to relax upon condensation, and hence the majority of the deposited film appears to be in the zb lattice. This is accompanied by an increase in the crystallinity parameter and a decrease in the antisites concentrations. However, a thin amorphous region was still nucleated at the surface. This amorphous region would have expanded had the growth simulation continued.

When the deposition rate was further reduced to ~ 5 nm/ns, Fig. 2(b), adatoms further relaxed upon condensation. While the surface region is still amorphous, it is thinner than that seen in Fig. 2(c). This is consistent with a further increase in the crystallinity parameter and a decrease in the antisites defect concentrations.

Finally, when the deposition rate was reduced to ~ 3 nm/ns, Fig. 2(a), adatoms fully relaxed to the zb lattice sites upon condensation. Correspondingly, the film exhibits highly crystalline zb structure. It is also associated with the highest crystallinity parameter ($\xi \sim 0.8$), and the lowest antisites defect concentrations. Note that $\xi = 1$ corresponds to an ideal zb crystal at a temperature of 0 K. Fig. 2(a) suggests that at a temperature of 1200 K, $\xi \sim 0.8$ would already correspond a highly crystalline film. Fig. 2(a) also suggests that at a substrate temperature of 1200 K, a deposition rate of ~ 3 nm/ns is likely to be lower than the critical deposition rate for meaningful MD simulations of CdTe vapor deposition.

2. Crystallinity and stoichiometry trend

The configurations shown in Fig. 2 qualitatively enable the film quality to be visualized. To further explore the film quality and defects, quantitative parameters ξ for measuring film crystallinity, X for measuring stoichiometry were calculated according to the definition discussed in Appendix. Here we exclude 5% of deposited atoms on the surface in the calculations. The results for the crystallinity and stoichiometry parameters obtained for all the simulated films are shown in Fig. 3 as a function of deposition rate. In Fig. 3 and the following figures (Figs. 4, 8, 9, 10, 12, 14), the lines are not fitted but are rather used to guide eyes. It can be seen that in general reducing the deposition rate resulted in a continuous improvement of crystallinity within the deposition rate range between 2 and 14 nm/ns. In particular, a critical deposition rate of around 3 nm/ns corresponding to a high crystallinity parameter of $\xi \sim 0.8$ can be obtained from Fig. 3. On the other hand, Fig. 3 shows that the film stoichiometry is close to the ideal value of one for the entire deposition rate range explored, suggesting that the film stoichiometry may be primarily determined by the vapor species ratio (the vapor species ratio used here is Te:Cd = 1) and less sensitive to the deposition rate.

3. Antisite concentration trend

The fraction of Cd@Te and Te@Cd antisites with respect to number of lattice sites in the deposited films were also calculated to quantify the deposition rate effect on defect incorporation. Again the 5% of deposited atoms on the surface were excluded in the calculations. The results are shown in Fig. 4. It can be seen that in general the antisites defect concentrations continuously decreased as the deposition rate was reduced. This is because the antisites are associated with high energies and are not stable configurations. When the deposition rate was high, the high energy surface antisites did not have sufficient time to reconstruct to lower energy configurations before being buried. As a result, high antisite defect concentrations were obtained. When the deposition rate was reduced, these defects could reconstruct to lower energy zb configurations, resulting in the reduction of the antisites concentrations.

B. Deposition species effects

While CdTe films are usually grown from atomic Cd and molecular Te_2 vapor species [], they can also be grown from all atomic vapor species. To explore if the species of vapor phases can affect the film structures, simulations were performed using atomic forms of Cd and Te adatoms at a substrate temperature of 1200 K, a deposition rate near 2 nm/ns, a Te:Cd vapor species ratio of 1, and two adatom energies of 0.1 and 1.0 eV. The configurations obtained are shown in Figs. 5(a) and 5(b) for the adatom energies of 0.1 and 1.0 eV respectively. Comparison of Fig. 5(a) and Fig. 2(a) indicates that the film structure obtained using the atomic tellurium species is relatively less crystalline. This is consistent with smaller crystalline parameter ξ, less stoichiometric parameter X, and high antisite concentrations $f_{Cd@Te}$ and $f_{Te@Cd}$ in the atomic case than in the molecular case. Note that when a Te_2 molecule is condensed on a surface, it is readily dissociated into two Te atoms. This dissociation absorbs energy from the surface and two closely

separated Te atoms also provide strong bonding to the nearby Cd atoms (Cd-Te interaction is relatively stronger). This would reduce the re-evaporation of the volatile cadmium. On the other hand, the impact energy of an atomic Te adatom may promote the evaporation of cadmium. This can be verified from Fig. 5(a), where the stoichiometry parameter is noticeably larger than the ideal value of one (i.e., Cd depletion), and the overall deposition rate is also smaller than that in Fig. 2(a) under the condition that the adatom injection frequencies are the same in both cases. Because the film obtained using the atomic Te vapor species is not in an ideal stoichiometry, it is not surprising that it is associated with a reduced crystallinity and increased antisite defect concentrations.

Comparison of Fig. 5(b) with Fig. 5(a) indicates that increasing the adatom energy does not significantly change the film structure except that Fig. 5(b) has a flatter surface than Fig. 5(a) due to an impact induced flattening effects [45,46]. Interestingly, Fig. 5(b) shows the evaporation of some Te_2 molecules. It suggests that while only atomic Te vapor species was used in simulations, the excess Te atoms on the surface can recombine to form molecules and in the high energy conditions, re-evaporate into the vapor. This finding is in good agreement with the common knowledge that Te_2 vapor is a relatively stable phase [].

C. Adatom energy effects

While the adatom energy in the thermal evaporation deposition processes is usually limited to around 0.1 eV, many sputter deposition processes enable adatom energy to be controlled from thermal energy to above 1.0 eV. Fig. 5 already explored the adatom energy effects using the atomic Te vapor species. To further examine if adatom energy can have a significant effect on the quality of CdTe films, simulations were performed at a substrate temperature of 1200 K, a deposition rate near 2.7 nm/ns, a Te:Cd vapor species ratio of one, a molecular Te_2 vapor

species, and various adatom energies between 0.1 and 1.0 eV. The resulting atomic configurations obtained at two adatom energies of 0.6 and 1.0 eV are shown respectively in Figs. 6(a) and 6(b). Figs. 2(a), Figs. 6(a) and 6(b) all indicate that the atomic scale structures, the film crystallinity ξ, the stoichiometry parameter X, the antisites fractions $f_{Cd@Te}$ and $f_{Te@Cd}$ are all comparable and therefore insensitive to the adatom energy. This also means that the thermally activated diffusion processes may be more important in controlling the structures of the CdTe films than the adatom energy induced short-time impact processes.

D. Deposition temperature effects

Substrate temperature and vapor phase species ratio (representing the chemical potential of the species in the vapor) are the two primary processing conditions for vapor deposition of semiconductor compounds. Here we first explore the effect of substrate temperature.

1. Atomic structure observation

Simulations were performed at a deposition rate near 3 nm/ns, a Te:Cd vapor species ratio of 1, a molecular Te_2 vapor species, an adatom energy of 0.1 eV, and various substrate temperatures between 500 and 1200 K. The atomic configurations at four selected substrate temperatures of 700, 900, 1000, and 1100 K are shown in Figs. 7(a) – 7(d) respectively. It can be seen that at the simulated low substrate temperature of 700 K, Fig. 7(a), the film was largely amorphous. This is because the critical deposition rate for crystalline growth is below 3 nm/ns at 700 K. When the temperature was increased to 900 K, Fig. 7(b), a majority of the film became crystalline except that a thin surface layer still retained some irregular features. When the substrate temperature was further increased to 1000 K, Fig. 7(c), the irregular layer at the surface became thinner. Finally, when the substrate temperature was increased to 1100 K, Fig. 7(d), the entire film became highly crystalline. These observations verify that as temperature was

increased, adatoms became increasingly mobile and therefore were more likely to relax to the low energy lattice sites on a short time scale. Hence, increasing substrate temperature has a similar effect to decreasing the deposition rate as shown in Fig. 2.

2. Crystallinity trend

To get a more quantitative picture of the temperature effect on film structure, the crystallinity and stoichiometry parameters were calculated for all the substrate temperatures and the results are shown in Fig. 8 using the filled diamonds and filled circles to represent respectively the crystallinity and stoichiometry parameters. As discussed above, the deposition rate used in the simulations is accelerated so that the diffusion distance of surface atoms is underestimated. This problem can be mitigated using elevated substrate temperatures to accelerate the surface diffusion. As a first order approximation, the simulated substrate temperature T at the simulated deposition rate R can be converted to a temperature T_x that corresponds to a different deposition rate R_x by equating the diffusion distances of surface atoms obtained under the two different deposition rates [47]:

$$T_x = \frac{T}{\frac{k \cdot T}{Q} \ln\left(\frac{R}{R_x}\right) + 1}. \quad (1)$$

where k is Boltzmann constant, and Q is activation energy barrier of surface diffusion. Our calculations indicated that the diffusion barriers for Cd on a Te terminated surface and Te on Cd terminated surface are ?? and ?? eV respectively. Using Q = ?? eV, Eq. (1) can be used to convert the results obtained at different deposition rates and a constant temperature of 1200 K (Figs. 3-4) to those at different temperatures and a constant deposition rate of around 3 nm/ns. The converted data are included in Fig. 8 using the unfilled diamonds and unfilled circles to represent respectively the crystallinity and stoichiometry parameters. It can be seen that the

unfilled diamonds and unfilled circles mesh well with the filled diamonds and filled circles, suggesting that Eq. (1) might be a reasonable approximation. Based on Eq. (1), the simulated temperatures are converted to the experimental temperatures assuming an experimental deposition rate of about $R_x = 10^7 \cdot R$. The resulting estimated experimental temperature range is marked in Fig. 8 for reference. For clarity, however, the following analysis all uses the simulated temperature.

It can be seen that at the deposition rate of 3 nm/ns, the crystallinity is very poor (ξ equals 0.3 or below) when the substrate temperature is below 700 K. As temperature is increased from 700 K, the crystallinity first undergoes a sharp improvement and then reaches a saturated value around 0.8 at a substrate temperature of 900 K. This indicates that at the chosen simulated deposition rate of 3 nm/ns, MD simulations of vapor deposition of CdTe films must be carried out at substrate temperatures above 900 K for the results to be meaningful. Fig. 8 also indicates that at the low simulated substrate temperatures, say, 500 K, the stoichiometry of the films is significantly below the ideal value of one at the stoichiometric vapor ratio Te:Cd = 1. Increasing the substrate temperature increasingly causes the film stoichiometry to approach the ideal value. The lower film stoichiometry at low substrate temperatures indicates that the sticking of the tellurium vapor species on the growth surface is lower than that of the cadmium species. The low stoichiometry (Te-depletion) of the films promotes the formation of defects such as Te vacancies, Cd@Te antisites, and Cd interstitials. In general, the sticking of tellurium and cadmium atoms can be both maximized if the growth zb CdTe film is ideally stoichiometric because this phase is the most stable. This means that if the film is Cd-rich, the evaporation of Cd becomes more significant than that of Te; and likewise, if the film is Te-rich, the evaporation of Te becomes more significant than that of Cd. Increasing the substrate temperature promotes

this process towards equilibrium, and therefore results in more stoichiometric films.

3. Antisite concentration trend

The Cd@Te and Te@Cd antisite concentrations were also calculated and the results are shown as a function of substrate temperature in Fig. 9. It can be seen that the two antisite concentrations both decrease as the substrate temperature is increased. This can be attributed to two mechanisms. First, the improvement in film stoichiometry due to the increase in substrate temperature naturally results in the reduction in the antisites concentrations. Second, the antisites are associated with higher energies. The increase in substrate temperature increases the mobility of surface atoms to anneal out these higher energy defects before they are buried into the bulk part of the films.

4. Sticking coefficient trend

To understand interactions between vapor and the growth surface, the sticking probability of the deposited atoms were calculated. The results are plotted as a function of substrate temperature in Fig. 10. It can be seen that as expected, the sticking probability was increasingly reduced as the substrate temperature was increased. In particular, our more detailed analysis indicated that the Te sticking probability is lower on a Te-rich surface than a Cd-rich surface, and the Cd sticking probability is lower on a Cd-rich surface than a Te-rich surface. Increasing substrate temperature promotes this effect, and hence provides a mechanism to improve film stoichiometry and to reduce defect concentrations.

E. Vapor phase species ratio effects

Vapor species ratio is another important processing condition for the vapor deposition of semiconductor compound as it directly controls the stoichiometry of the films. Here, we explore the vapor species ratio effects.

1. Atomic structure observation

Simulations were performed at a deposition rate near 3 nm/ns, two substrate temperatures of 1000 and 1200 K, a molecular Te_2 vapor species, an adatom energy of 0.1 eV, and various vapor species ratios between Te:Cd = 0.8 and Te:Cd = 1.5. Selected atomic configurations at two Te:Cd vapor species ratios of 0.8 and 1.2 and the two substrate temperatures of 1000 and 1200 K are compared in Fig. 11. Fig. 11 indicates that at the lower temperature of 1000 K, the film obtained under the Cd-rich vapor condition (Te:Cd = 0.8) has a pretty sharp crystalline structure, Fig. 11(c). This means that the excess Cd atoms deposited on the surface can re-evaporate into the vapor at 1000 K. It is not surprising because Cd is rather volatile with a low cohesive energy of -1.133 eV/atom [49]. The crystalline quality of the film becomes significantly reduced under the Te-rich (Te:Cd = 1.2) vapor growth condition at 1000 K, Fig. 11(d). This means that the excess Te atoms deposited on the surface cannot be fully re-evaporated at 1000 K. Contrarily, the crystalline quality is high at the higher temperature of 1200 K under both Cd-rich and Te-rich vapor growth conditions. This means that at 1200 K, the re-evaporation of excess species on the growth surface is significant even for the less volatile Te, thereby promoting the formation of stoichiometric films.

2. Crystallinity trend

The crystallinity and stoichiometry parameters were again calculated and the results are shown in Fig. 12 as a function of vapor phase Te:Cd ratio at two substrate temperatures of 1000 and 1200 K. It can be seen that at both temperatures, the crystallinity reaches peak value of

approximately 0.8 at the Te:Cd vapor species ratio between 0.9 and 1.1. This is expected because the stoichiometric vapor ratio is most likely to result in stoichiometric film composition required for highly crystalline CdTe compound. Interestingly, the decrease in the film crystallinity is more significant under the Te-rich vapor condition than under the Cd-rich condition at the low temperature of 1000 K. This is because the excess Cd is more likely to re-evaporate as described above. The difference between the Cd-rich and Te-rich vapor conditions is seen to become smaller at the high substrate temperature of 1200 K. This occurs because the excess Te can also easily re-evaporate at the high temperature.

As expected, Fig. 12 also indicates that an increase in the vapor phase Te:Cd ratio continuously results in an increase in the Te:Cd ratio in the deposited films, and the stoichiometric film composition occurs when the vapor Te:Cd ratio is close to (but slightly less than) unity. Furthermore, increasing the substrate temperature causes the film composition to be closer to the stoichiometric value at various vapor Te:Cd ratios. This is consistent with the discussion above that the high temperature induced evaporation helps adjust the film composition towards to the stoichiometric value.

3. Antisite concentration trend

The Cd@Te and Te@Cd antisite concentrations were calculated and the results are shown in Fig. 13 as a function of the vapor Te:Cd ratio for the two substrate temperatures. It can be seen that the two antisite concentrations both reach the minimum at the stoichiometric vapor Te:Cd ratio near unity. The increase in the antisite concentrations due to a reduction in the vapor Te:Cd ratio is relatively insignificant than that due to an increase in the vapor Te:Cd ratio especially at the relatively low temperature of 1000 K. This confirms the discussion above that the film structure is more tolerant to the Cd-rich growth condition because the excess Cd atoms on the

surface can readily re-evaporate, and the high temperatures promote the stoichiometric films under the Te-rich growth conditions because it enables the excess Te atoms on the surface to also re-evaporate.

4. Sticking coefficient trend

The sticking probability of the deposited atoms was calculated and the results are plotted as a function of vapor Te:Cd ratio in Fig. 14 for the two substrate temperatures. It can be seen that at the relatively low temperature of 1000 K, increasing the vapor Te:Cd ratio from 0.8 to 1.5 continuously increases the sticking probability. This is because at the Cd-rich deposition condition of vapor Te:Cd ratio near 0.8, the growth surface has excess Cd. The volatile Cd easily re-evaporates resulting in a low sticking coefficient. As the vapor Te:Cd ratio increases, the surface becomes increasingly Te-rich. Because the Te atoms are less likely to re-evaporate, the sticking probability increases. Different situation arises at the relatively high substrate temperature of 1200 K where the sticking is seen to reach a maximum value at a vapor Te:Cd ratio near 1.2. At 1200 K, both excess Cd and excess Te atoms on the surface can re-evaporate. Only when the surface forms the lowest energy stoichiometric CdTe compound, or the Te surface atoms are not too excessive, will the re-evaporation be low. This accounts for Fig. 14 and the other observations mentioned above.

IV. CONCLUSIONS

Molecular dynamics simulations of crystalline growth of CdTe are interesting due to the important photovoltaic and radiation detection applications of the material. This work describes a molecular dynamics method for simulating the crystalline growth of the CdTe films during vapor deposition using the most fundamental analytical interatomic potential currently available: the bond order potential. While our case simulations were performed on a relatively small scale

using serial MD codes, they proved that a well parameterized BOP can predict the crystalline growth during vapor deposition simulations and at the same time accurately predict the energy spectrum of a variety of elemental and compound phases as well as various defects. While more interesting studies of defect formation mechanisms belong to a separate effort employing massively parallel MD simulations on a large scale, our extensive small simulations also result in the following conclusions:

(i) For the MD simulations to predict crystalline growth, the deposition rates need to be below ~ 3nm/ns and the substrate temperatures need to be above 900 K, Fig. 8. The unrealistic simulated condition, however, can be reasonably related to realistic conditions through Eq. (1);

(ii) If atomic Te vapor is used instead of the molecular Te_2 vapor, then the vapor Te/Cd needs to be reduced. This is consistent with keeping the tellurium chemical constant;

(iii) Adatom energy does not sensitively affect the film structure;

(iv) A vapor Te:Cd ratio of near unity is ideal to create stoichiometric CdTe films. Otherwise vapor Te:Cd ratio below one is more likely to produce stoichiometric CdTe films than above one because excess Cd atoms are more likely to re-evaporate than excess Te atoms. Tolerance on the vapor species ratio is improved by increasing the substrate temperature where both excess Cd and excess Te atoms on the surface can re-evaporate.

ACKNOWLEDGEMENTS

This work is supported by the NNSA/DOE Office of Nonproliferation Research and Development, Proliferation Detection Program, Advanced Materials Portfolio, and The National Institute for Nano-Engineering (NINE). Sandia National Laboratories is a multi-program

laboratory managed and operated by Sandia Corporation, a wholly owned subsidiary of Lockheed Martin Corporation, for the U.S. Department of Energy's National Nuclear Security Administration under contract DE-AC04-94AL85000.

APPENDIX: CRYSTALLINITY AND STOICHIOMETRY PARAMETERS

A crystallinity parameter capable of quantifying the level of closeness of the deposited film to an ideal crystal is needed. Suppose that a given adatom i has a set of nearest neighbor atoms whose positions are notated as $\{\mathbf{r}_i\}$. If the center atom i is assumed to be at a lattice site, then a set of nearest neighbor lattice sites can be determined based on the substrate orientation and lattice constants. The positions of these lattice sites that most closely match $\{\mathbf{r}_i\}$ are notated as $\{\mathbf{R}_i\}$. The mean square deviation of $\{\mathbf{r}_i\}$ from $\{\mathbf{R}_i\}$, $\Delta_i = \langle(\mathbf{R}_i - \mathbf{r}_i)^2\rangle$, represents the deviation of atom i's environment from the crystalline configuration. A parameter, $\xi_i = \exp(-\alpha \cdot \Delta_i)$, which equals 1 at $\Delta_i = 0$ and continuously drops to zero when Δ_i is increased, can then be used to characterize the crystallinity of atom i. Here we chose $\alpha = 1$. The crystallinity of the film can then be well described by the average crystallinity of deposited atoms, $\xi = \sum_i \xi_i$ /N, where N is the total number of the deposited atoms included in the summation. An ideal crystal at 0 K (i.e., no thermal oscillation) corresponds to a value of $\xi = 1$.

The ratio of Te to Cd atoms in the deposited films, $X = N_{Te}/N_{Cd}$, can be used to measure stoichiometry of the film (may reflect concentrations of defects such as vacancies, antisites, and interstitials), where N_{Te} and N_{Cd} are respectively the total numbers of Te and Cd atoms in the deposited film.

Figure Captions

Fig. 1. Cohesive energies of a variety of Cd, Te, and CdTe phases calculated by various models.

Fig. 2. Effect of deposition rate on film configuration.

Fig. 3. Effect of deposition rate on film crystallinity and stoichiometry.

Fig. 4. Effect of deposition rate on film antisite concentration.

Fig. 5. Effect of tellurium vapor species (atomic Te or molecular Te_2) on film configuration.

Fig. 6. Effect of adatom energy on film configuration.

Fig. 7. Effect of substrate temperature on film configuration.

Fig. 8. Effect of substrate temperature on film crystallinity and stoichiometry.

Fig. 9. Effect of substrate temperature on film antisite concentration.

Fig. 10. Effect of substrate temperature on sticking coefficient.

Fig. 11. Effect of vapor phase Te:Cd ratio on film configuration.

Fig. 12. Effect of vapor phase Te:Cd ratio on film crystallinity and stoichiometry.

Fig. 13. Effect of vapor phase Te:Cd ratio on film antisite concentration.

Fig. 14. Effect of vapor phase Te:Cd ratio on sticking coefficient.

References

1 L. L. Kazmerski, *J. Elec. Spec. Related Phenomena.*, **150**, 105 (2006).
2 J. J. Loferski, *J. Appl. Phys.*, **27**, 777 (1956).
3 W. H. Bloss, F. Pfisterer, M. Schubert, and T. Walter, *Prog. Photovolt.*, **3**, 3 (1995).
4 M. D. G. Potter, M. Cousins, K. Durose, and D. P. Halliday, *J. Mater. Sci.: Mater. Elec.*, **11**, 525 (2000).
5 G. S. Khrypunov, E. P. Chernykh, N. A. Kovtun, and E. K. Belonogov, *Semiconductors*, **43**, 1046 (2009).
6 R. H. Bube, and K. W. Mitchell, *J. Electron. Mater.*, **22**, 17 (1993).
7 H. C. Chou, and A. Rohatgi, *J. Electron. Mater.*, **23**, 31 (1994).
8 T. E. Schlesinger, J. E. Toney, H. Yoon, E. Y. Lee, B. A. Brunett, L. Franks, and R. B. James, *Mater. Sci. Eng.*, **32**, 103 (2001).
9 P. J. Sellin, *Nuc. Instr. Meth. Phys. Res. A.*, **513**, 332 (2003).
10 A. Peurrung, *Mater. Today*, **11**, 50 (2008).
11 T. Takahashi, and S. Watanabe, *IEEE Trans. Nuc. Sci.*, **48**, 950 (2001).
12 A. Shah, P. Torres, R. Tscharner, N. Wyrsch, and H. Keppner, *Science*, **285**, 692 (1999).
13 J. D. Beach, and B. E. McCandless, *MRS Bull.*, **32**, 225 (2007).
14 K. D. Dobson, I. Visoly-Fisher, G. Hodes, D. Cahen, *Solar Ener. Mater. Solar Cells*, **62**, 295 (2000).
15 A. Rohatgi, R. Sudharsanan, S. A. Ringel, and M. H. MacDougal, *Solar Cells.*, **30**, 109 (1991).
16 J. Versluys, P. Clauws, P. Nollet, S. Degrave, and M. Burgelman, *Thin Solid Films*, **451-452**, 434 (2004).
17 Y. Yan, M. M. Al-Jassim, and K. M. Jones, *J. Appl. Phys.*, **94**, 2976 (2003).
18 A. E. Bolotnikov, G. S. Camarda, G. A. Carini, Y. Cui, L. Li, and R. B. James, *Nucl. Instru. Meth. Phys. Res. A*, **579**, 125 (2007).
19 A. E. Bolotnikov, G. S. Camarda, G. A. Carini, Y. Cui, L. Li, and R. B. James, *Nucl. Instru. Meth. Phys. Res. A*, **571**, 687 (2007).
20 C. Szeles, *Phys. Stat. Sol. A*, **241**, 783 (2004).
21 C. Szeles, *IEEE Trans. Nuc. Sci.*, **51**, 1242 (2004).
22 G. Zha, W. Jie, T. Tan, and L. Wang, *Phys. Stat. Sol. A*, **204**, 2196 (2007).
23 Z. Q. Wang, D. Stroud, and A. J. Markworth, *Phys. Rev. B*, **40**, 3129 (1989).
24 J. Oh, and C. H. Grein, *J. Cryst. Growth*, **193**, 241 (1998).
25 J. Wang, and A. Rockett, *Phys. Rev. B*, **43**, 12571 (1991).
26 D. K. Ward, X. W. Zhou, B. M. Wong, F. P. Doty, and J. A. Zimmerman, submitted.
27 F. H. Stillinger, and T. A. Weber, *Phys. Rev. B*, **31**, 5262 (1985).
28 J. Tersoff, *Phys. Rev. B*, **39**, 5566 (1989).
29 D. W. Brenner, *Phys. Rev. B*, **42**, 9458 (1990).
30 D. G. Pettifor, M. W. Finnis, D. Nguyen-Manh, D. A. Murdick, X. W. Zhou, and H. N. G. Wadley, *Mater. Sci. Eng. A*, **365**, 2 (2004).
31 D. G. Pettifor, and I. I. Oleinik, *Phys. Rev. B*, **59**, 8487 (1999).
32 D. G. Pettifor, and I. I. Oleinik, *Phys. Rev. Lett.*, **84**, 4124 (2000).
33 D. G. Pettifor, and I. I. Oleinik, *Phys. Rev. B*, **65**, 172103 (2002).
34 R. Drautz, D. Nguyen-Manh, D. A. Murdick, X. W. Zhou, H. N. G. Wadley, and D. G. Pettifor, *TMS Lett.*, **1**, 31 (2004).

35 R. Drautz, D. A. Murdick, D. Nguyen-Manh, X. W. Zhou, H. N. G. Wadley, and D. G. Pettifor, *Phys. Rev. B*, **72**, 144105 (2005).
36 D. A. Murdick, X. W. Zhou, H. N. G. Wadley, D. Nguyen-Manh, R. Drautz, and D. G. Pettifor, *Phys. Rev. B*, **73**, 45206 (2006).
37 D. Ward, X. W. Zhou, B. M. Wong, and F. P. Doty, *to be submitted to J. Appl. Phys*.
38 I. Barin, *"thermochemical data of pure substances"*, VCH, Weinheim, 1993.
39 S. B. Zhang and J. E. Northrup, *Phys. Rev. Lett.*, **67**, 2339 (1991).
40 J. E. Northrup and S. B. Zhang, *Phys. Rev. B*, **47**, R6791 (1993).
41 G.-X. Qian, R. M. Martin, and D. J. Chadi, *Phys. Rev. B*, **38**, 7649 (1988).
42 A. Nordieck, *Math, Comput.*, **16**, 22 (1962).
43 M. Parrinello, and A. Rahman, *J. Appl. Phys.*, **52**, 7128 (1981).
44 W. G. Hoover, *Phys. Rev. B*, **31**, 1695 (1985).
45 X. W. Zhou, H. N. G. Wadley, R. A. Johnson, D. J. Larson, N. Tabat, A. Cerezo, A. K. Petford-Long, G. D. W. Smith, P. H. Clifton, R. L. Martens, and T. F. Kelly, *Acta Mater.*, **49**, 4005 (2001)..
46 X. W. Zhou, and H. N. G. Wadley, *J. Appl. Phys.*, **84**, 2301 (1998).
47 X. W. Zhou, D. A. Murdick, B. Gillespie, and H. N. G. Wadley, *Phys. Rev. B*, **73**, 43337 (2006).
48 X. W. Zhou, and H. N. G. Wadley, *J. Appl. Phys.*, **84**, 2301 (1998).
49 I. Barin, "*Thermochemical data of pure substances"*, (VCH, Weinheim, 1993).

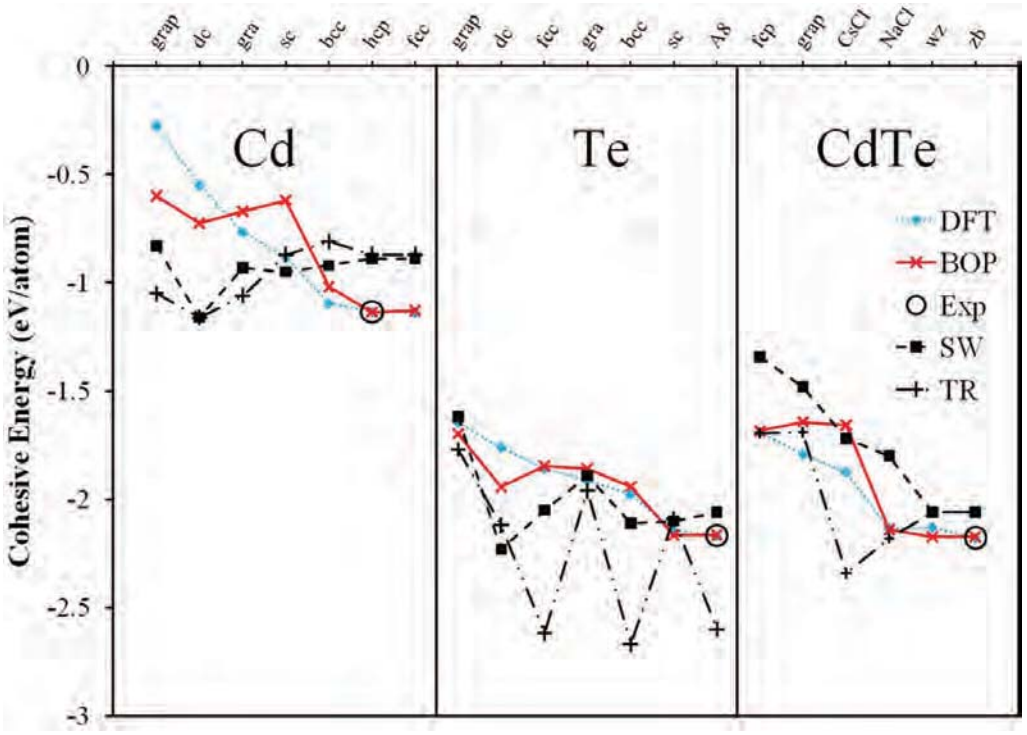
grap
dc
gra
sc
bcc
hcp
fcc
grap
dc
fcc
gra
bcc
sc
A8
fcp
grap
CsCl
NaCl
wz
zb
Cd
Te
CdTe
DFT
BOP
Exp
SW
TR
Cohesive Energy (eV/atom)
0
-0.5
-1
-1.5
-2
-2.5
-3

Figure 1

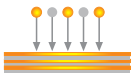

E_i = 0.1 eV
Te:Cd= 1
T = 1200 K
Te_2 vapor

(a) R ~ 2.7 nm/ns at t = 1.2 ns

y [001]

ξ ~ 0.81, X ~ 1.02, $f_{Cd@Te}$ = 0.002, $f_{Te@Cd}$ = 0.008

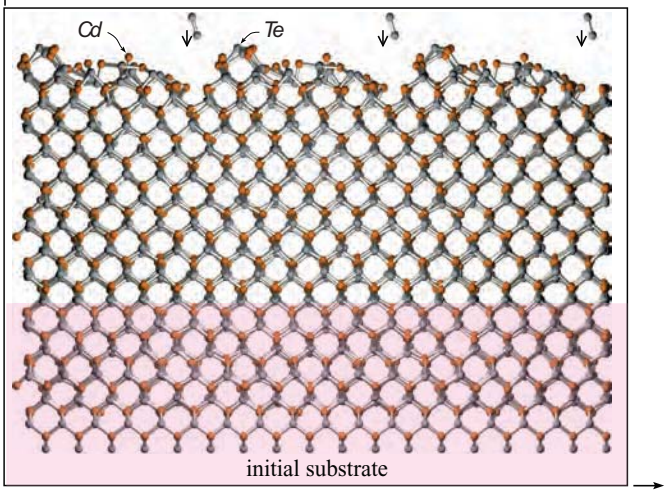

(b) R ~ 5.4 nm/ns at t = 0.6 ns

ξ ~ 0.76, X ~ 1.02, $f_{Cd@Te}$ = 0.012, $f_{Te@Cd}$ = 0.017

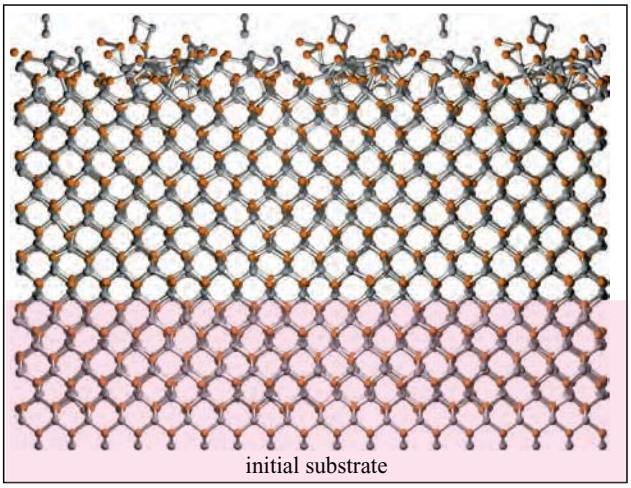

(c) R ~ 8.1 nm/ns at t = 0.4 ns

ξ ~ 0.69, X ~ 0.99, $f_{Cd@Te}$ = 0.027, $f_{Te@Cd}$ = 0.023

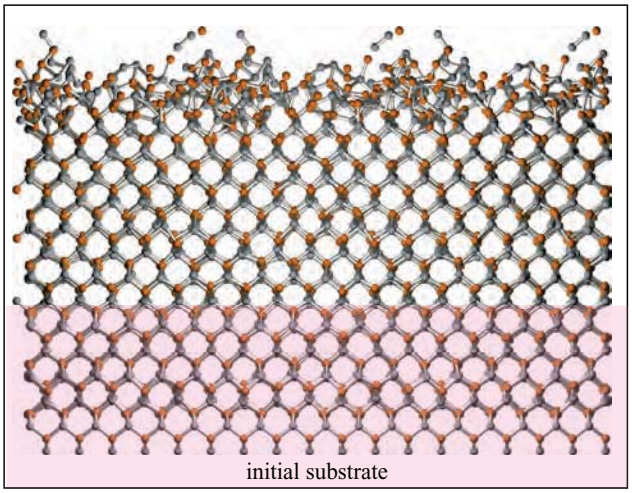

(d) R ~ 11.2 nm/ns at t = 0.3 ns

ξ ~ 0.45, X ~ 1.01, $f_{Cd@Te}$ = 0.075, $f_{Te@Cd}$ = 0.092

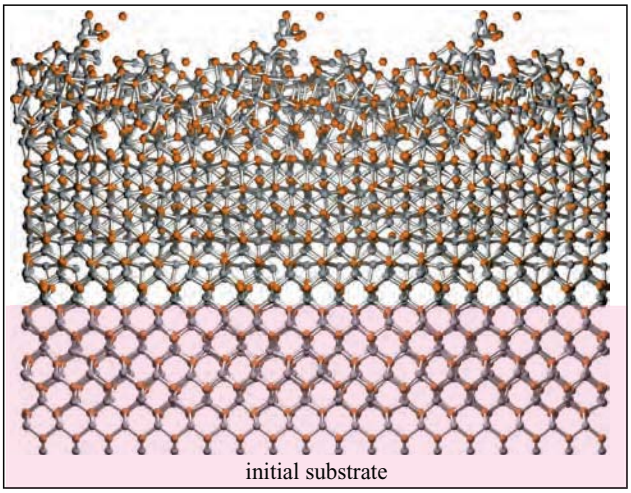

Figure 2

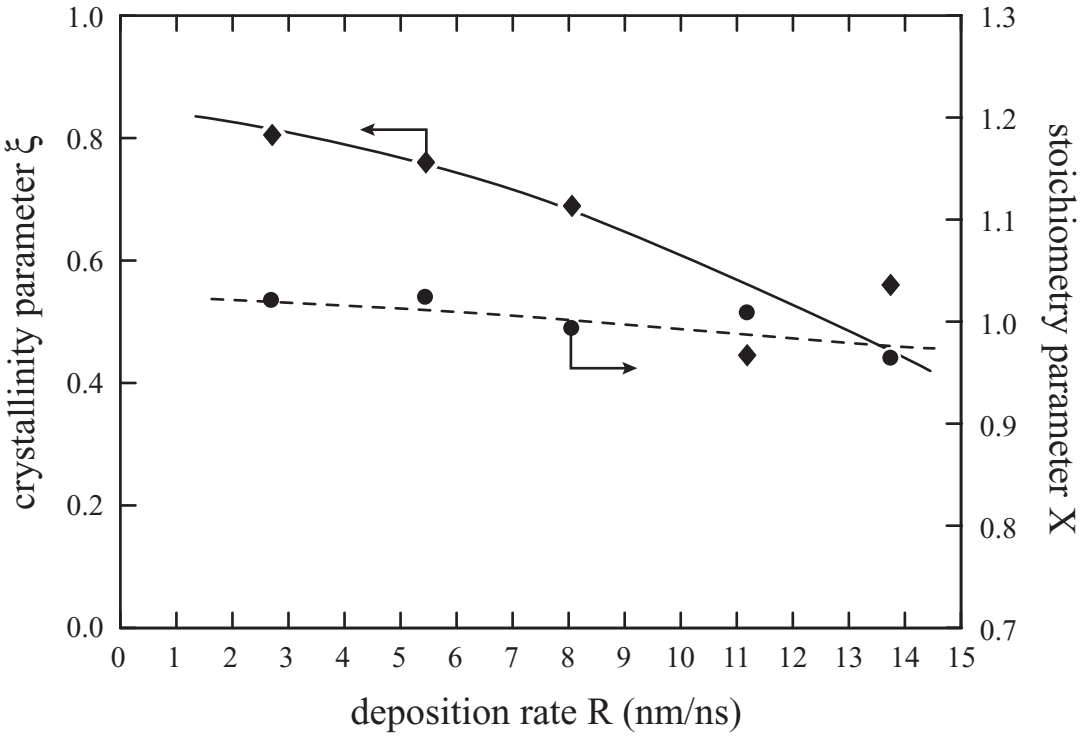
crystallinity parameter ξ
stoichiometry parameter X
deposition rate R (nm/ns)
1.0
0.8
0.6
0.4
0.2
0.0
1.3
1.2
1.1
1.0
0.9
0.8
0.7
0
1
2
3
4
5
6
7
8
9
10
11
12
13
14
15

Figure 3

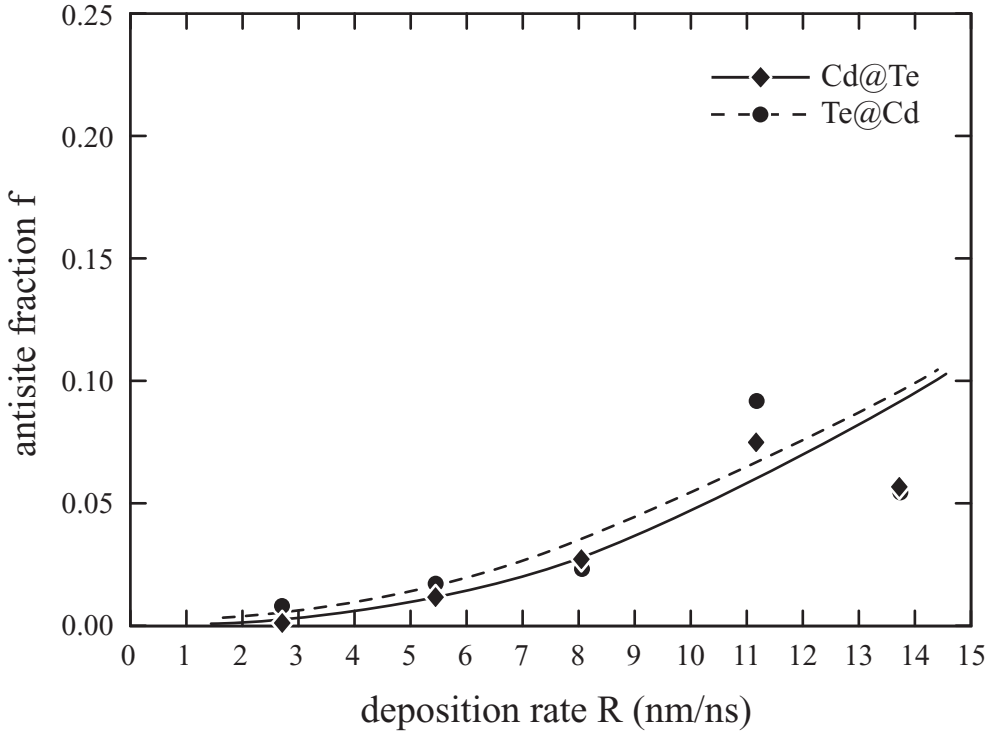
0.25
0.20
0.15
0.10
0.05
0.00
antisite fraction f
0
1
2
3
4
5
6
7
8
9
10
11
12
13
14
15
deposition rate R (nm/ns)
Cd@Te
Te@Cd

Figure

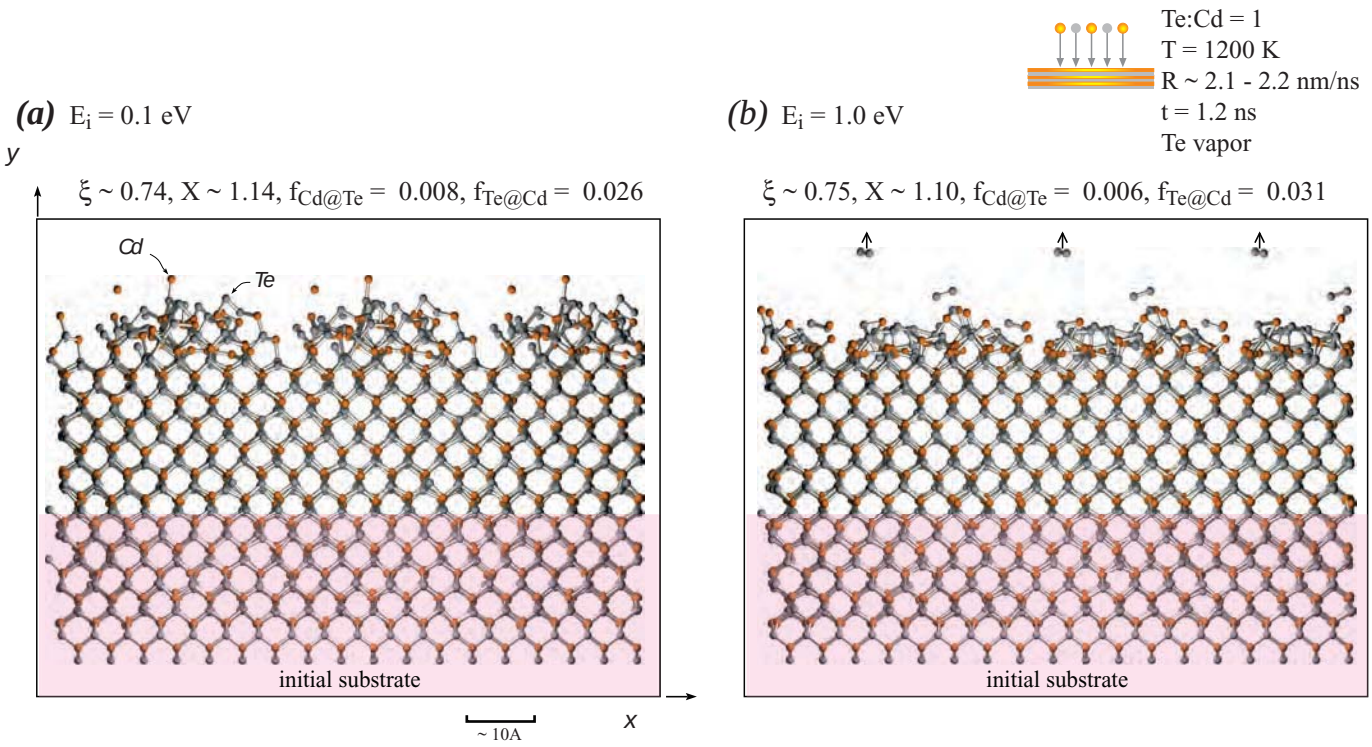
Te:Cd = 1
T = 1200 K
R ~ 2.1 - 2.2 nm/ns
t = 1.2 ns
Te vapor
(a) E_i = 0.1 eV
(b) E_i = 1.0 eV
y
ξ ~ 0.74, X ~ 1.14, f_Cd@Te = 0.008, f_Te@Cd = 0.026
ξ ~ 0.75, X ~ 1.10, f_Cd@Te = 0.006, f_Te@Cd = 0.031
Cd
Te
initial substrate
initial substrate
~ 10A
x

Figure

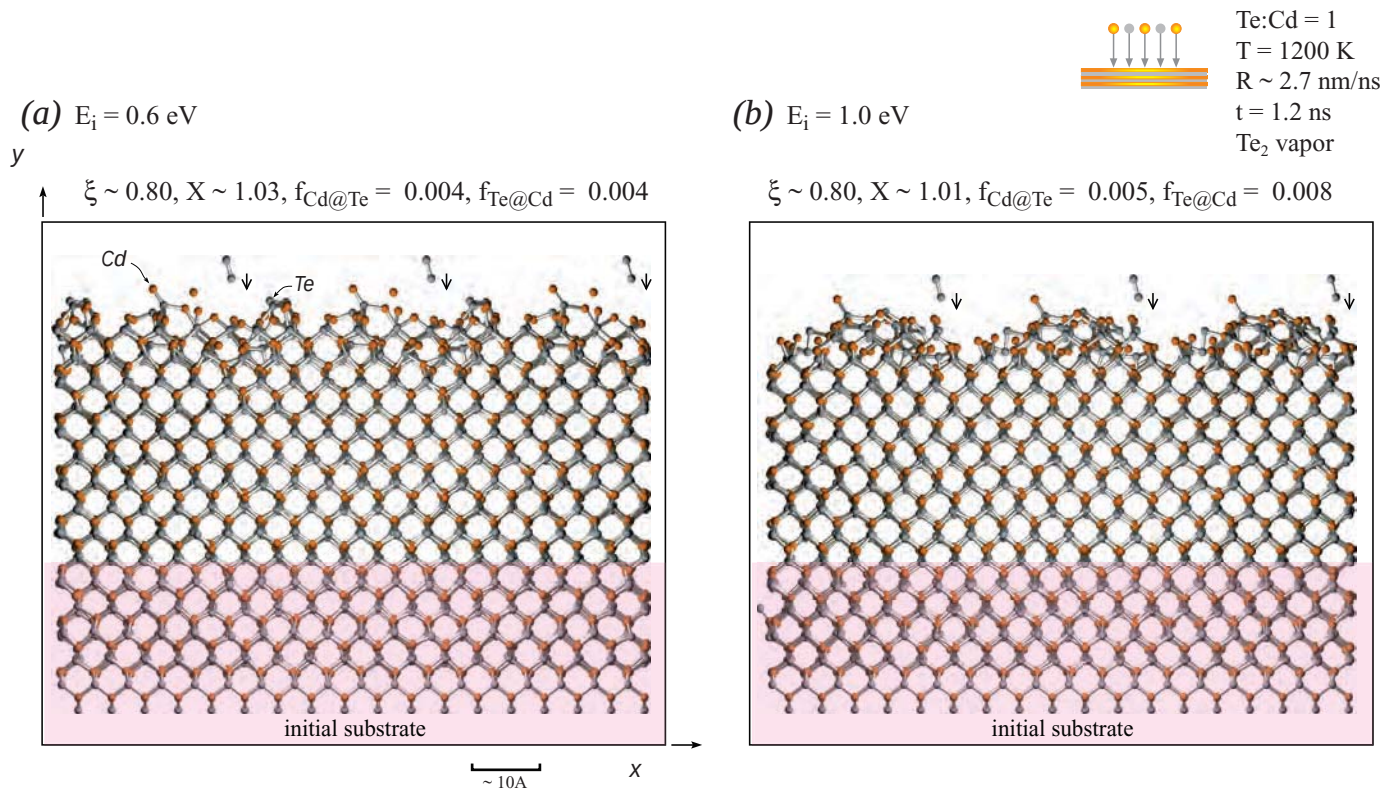
Te:Cd = 1
T = 1200 K
R ~ 2.7 nm/ns
t = 1.2 ns
Te2 vapor
(a) Ei = 0.6 eV
(b) Ei = 1.0 eV
y
ξ ~ 0.80, X ~ 1.03, fCd@Te = 0.004, fTe@Cd = 0.004
ξ ~ 0.80, X ~ 1.01, fCd@Te = 0.005, fTe@Cd = 0.008
Cd
Te
initial substrate
initial substrate
~ 10A
x

Figure

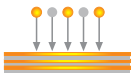

E_i = 0.1 eV
Te:Cd = 1
t = 1.2 ns
Te_2 vapor

(a) T = 700 K and R ~ 3.0 nm/ns

y

ξ ~ 0.28, X ~ 0.94, $f_{Cd@Te}$ = 0.149, $f_{Te@Cd}$ = 0.155

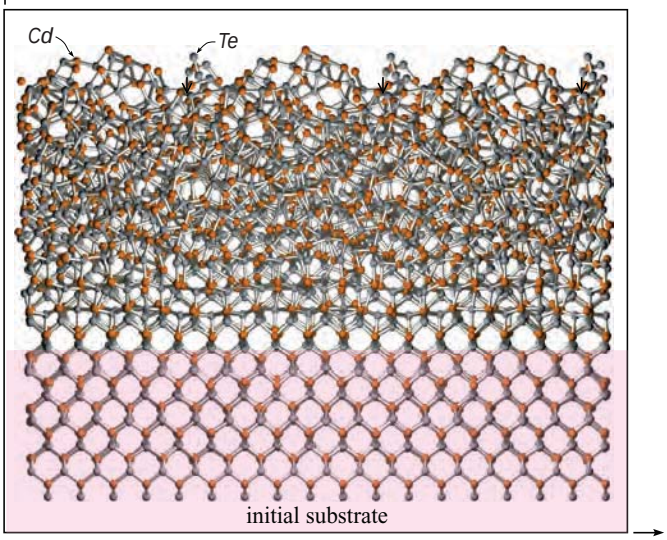

(b) T = 900 K and R ~ 2.9 nm/ns

ξ ~ 0.79, X ~ 0.99, $f_{Cd@Te}$ = 0.011, $f_{Te@Cd}$ = 0.011

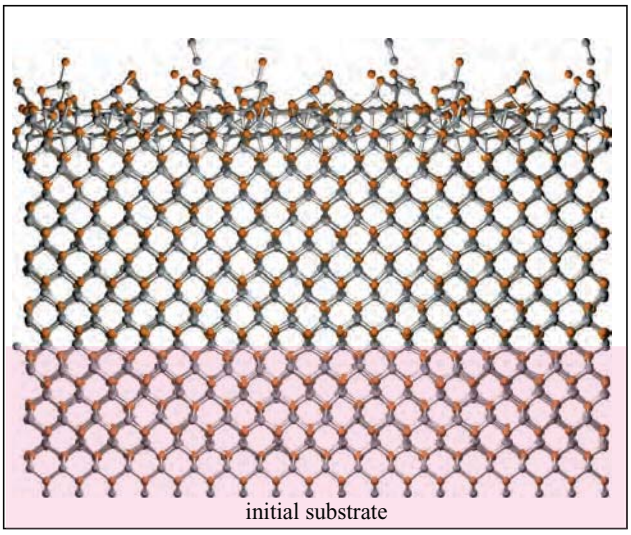

( ) T = 1000 K and R ~ 2.9 nm/ns

ξ ~ 0.81, X ~ 1.01, $f_{Cd@Te}$ = 0.007, $f_{Te@Cd}$ = 0.009

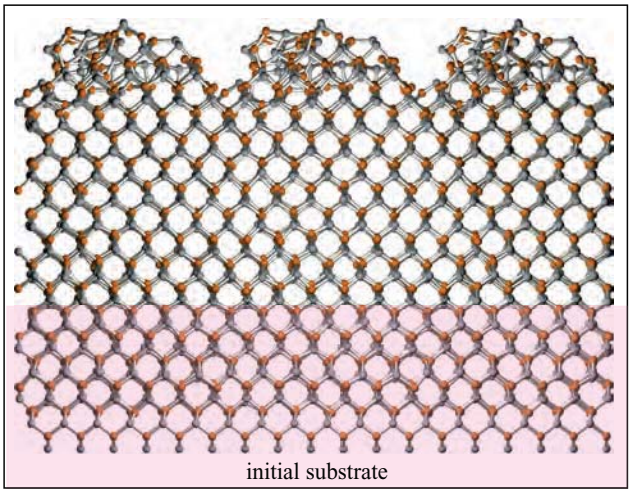

( ) T = 1100 K and R ~ 2.7 nm/ns

ξ ~ 0.81, X ~ 1.00, $f_{Cd@Te}$ = 0.002, $f_{Te@Cd}$ = 0.002

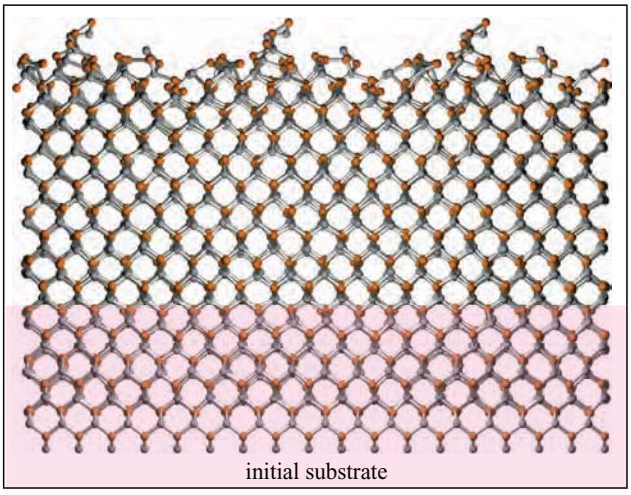

Figure

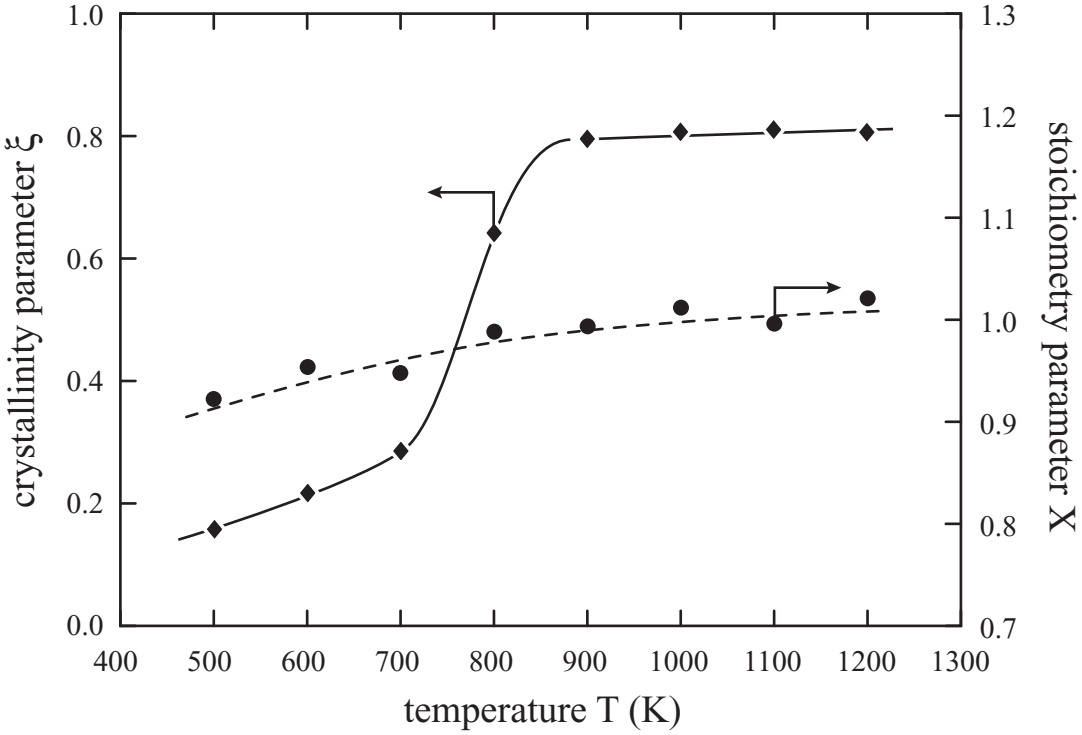
crystallinity parameter ξ
stoichiometry parameter X
temperature T (K)
1.0
0.8
0.6
0.4
0.2
0.0
1.3
1.2
1.1
1.0
0.9
0.8
0.7
400
500
600
700
800
900
1000
1100
1200
1300

Figure

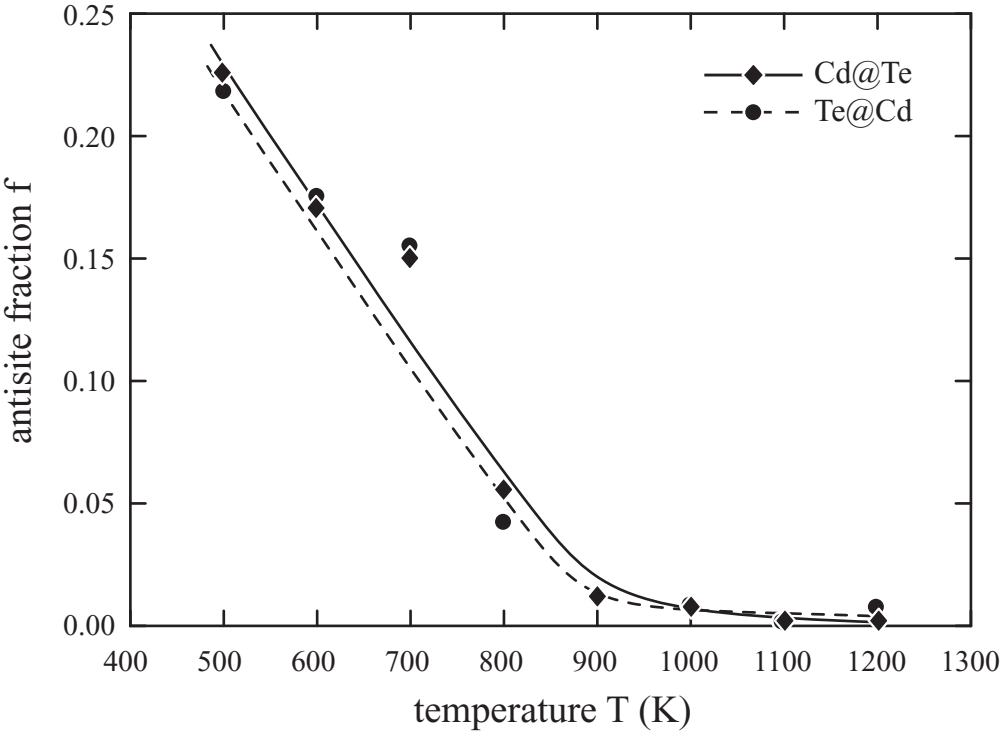
0.25
0.20
0.15
0.10
0.05
0.00
antisite fraction f
400
500
600
700
800
900
1000
1100
1200
1300
temperature T (K)
Cd@Te
Te@Cd

Figure

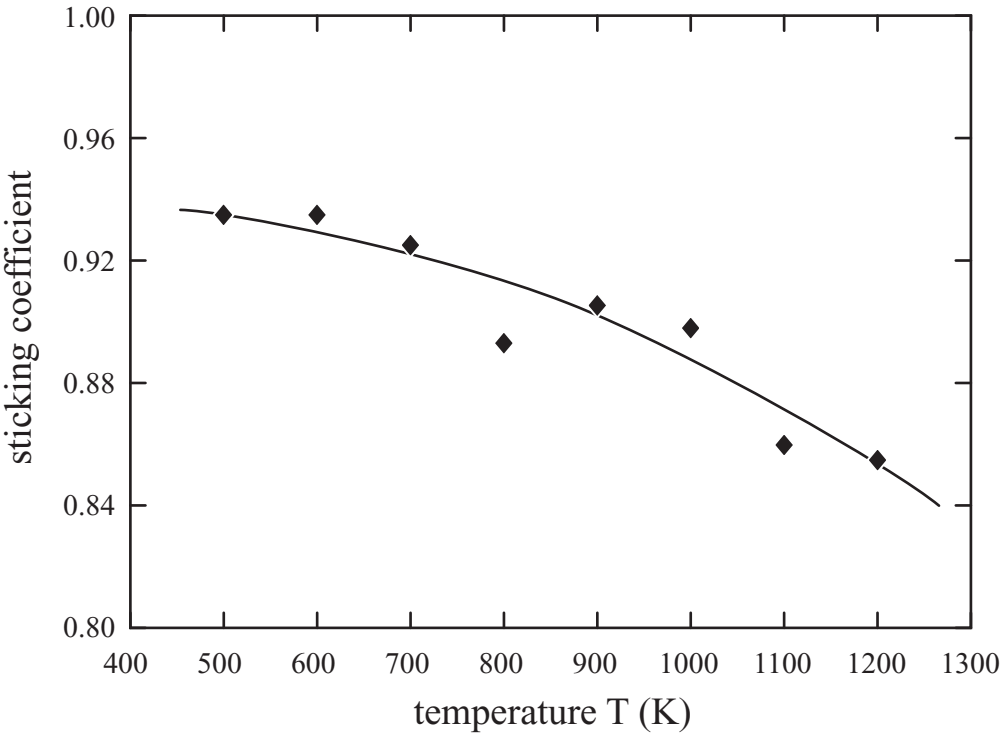
1.00
0.96
0.92
0.88
0.84
0.80
sticking coefficient
400
500
600
700
800
900
1000
1100
1200
1300
temperature T (K)

Figure

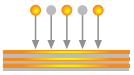

E_i = 0.1 eV
Te_2 vapor

(a) T = 1200 K, Te:Cd = 0.8, and R ~ 2.4 nm/ns

ξ ~ 0.75, X ~ 0.98, $f_{Cd@Te}$ = 0.015, $f_{Te@Cd}$ = 0.015

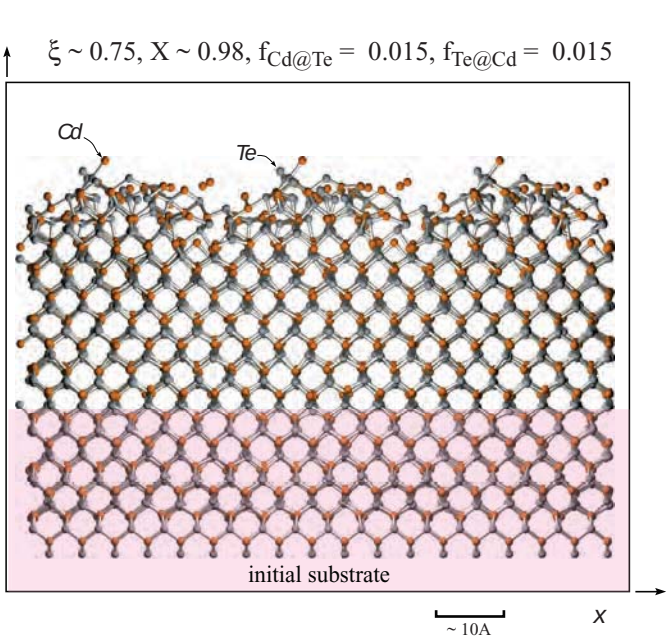

(b) T = 1200 K, Te:Cd = 1.2, and R ~ 2.9 nm/ns

ξ ~ 0.79, X ~ 1.09, $f_{Cd@Te}$ = 0.003, $f_{Te@Cd}$ = 0.021

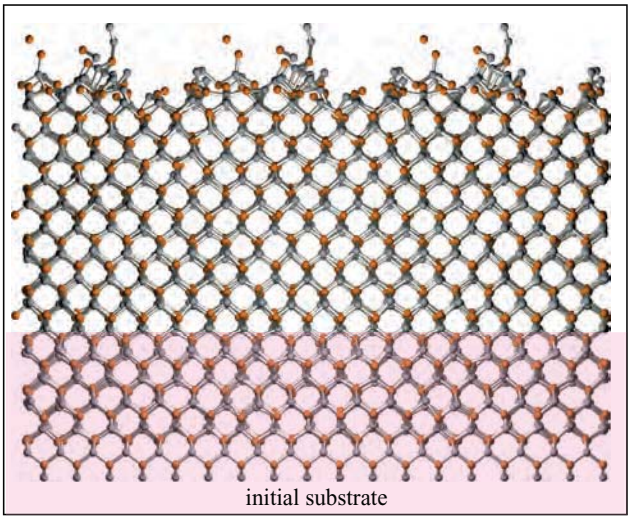

( ) T = 1000 K, Te:Cd = 0.8, and R ~ 2.5 nm/ns

ξ ~ 0.78, X ~ 0.95, $f_{Cd@Te}$ = 0.005, $f_{Te@Cd}$ = 0.005

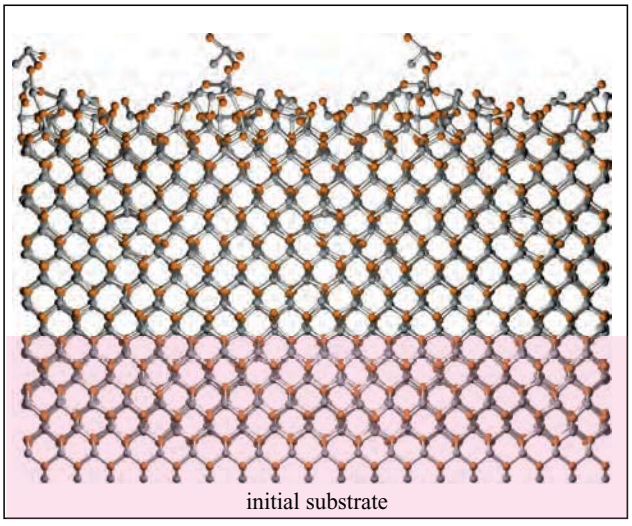

( ) T = 1000 K, Te:Cd = 1.2, and R ~ 3.08 nm/ns

ξ ~ 0.69, X ~ 1.11, $f_{Cd@Te}$ = 0.032, $f_{Te@Cd}$ = 0.045

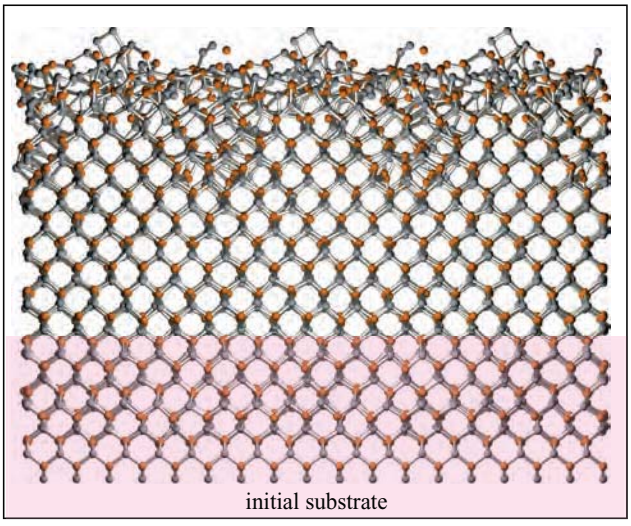

Figure

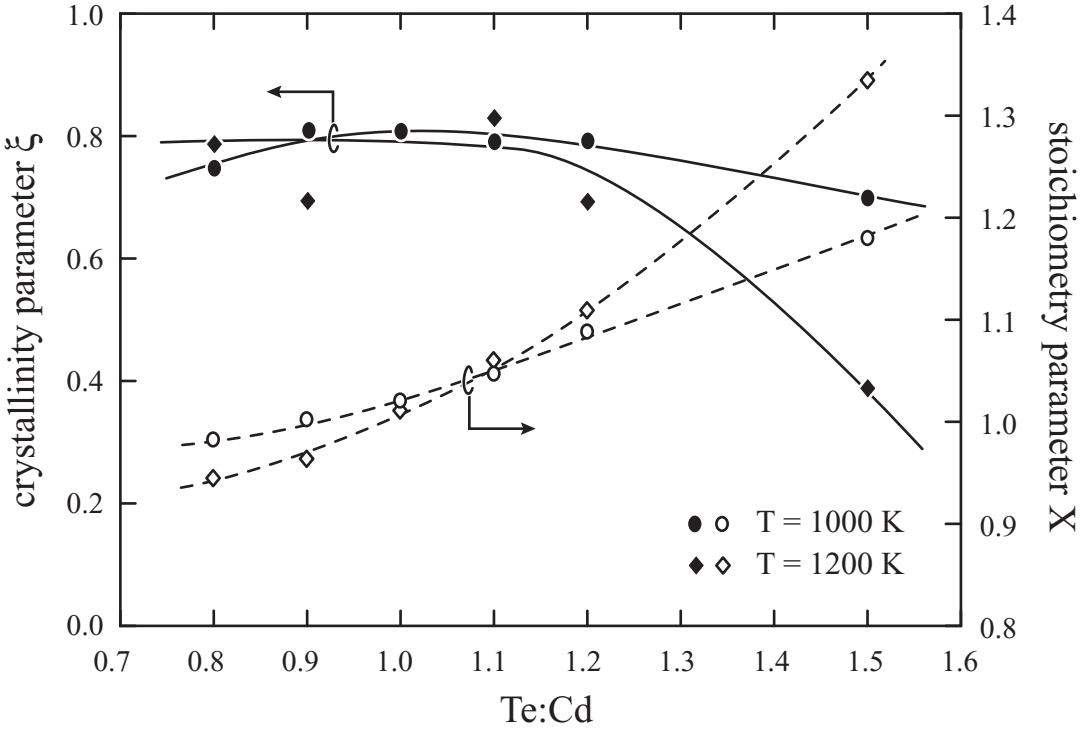
crystallinity parameter ξ
stoichiometry parameter X
Te:Cd
T = 1000 K
T = 1200 K
1.0
0.8
0.6
0.4
0.2
0.0
1.4
1.3
1.2
1.1
1.0
0.9
0.8
0.7
0.8
0.9
1.0
1.1
1.2
1.3
1.4
1.5
1.6

Figure

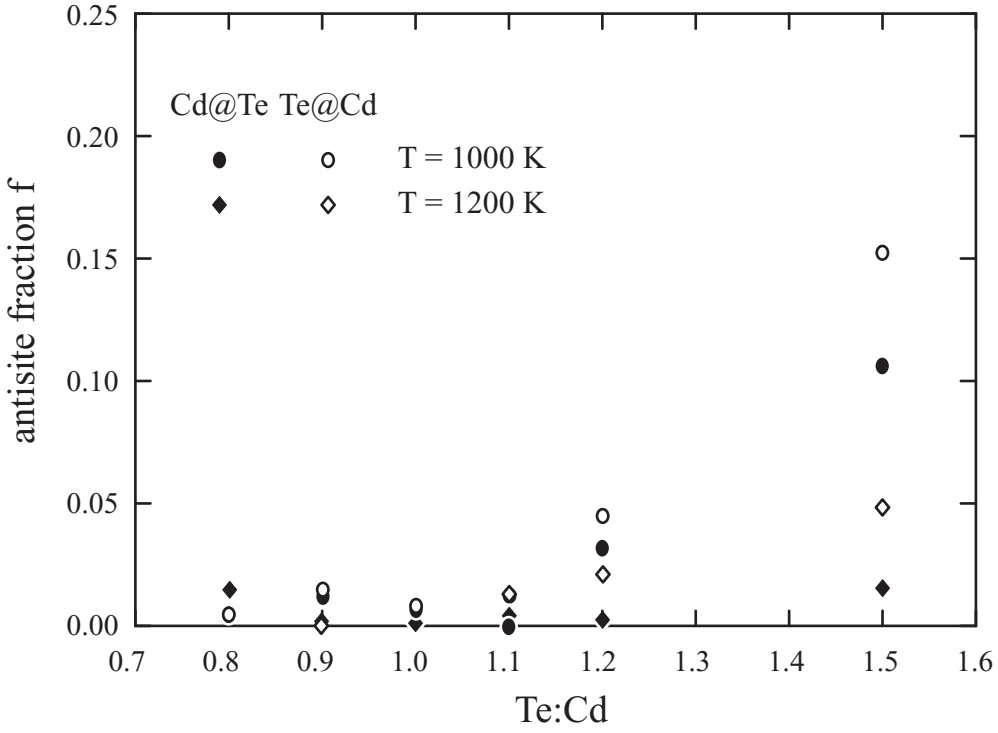
0.25
0.20
0.15
0.10
0.05
0.00
antisite fraction f
Cd@Te Te@Cd
T = 1000 K
T = 1200 K
0.7
0.8
0.9
1.0
1.1
1.2
1.3
1.4
1.5
1.6
Te:Cd

Figure 3

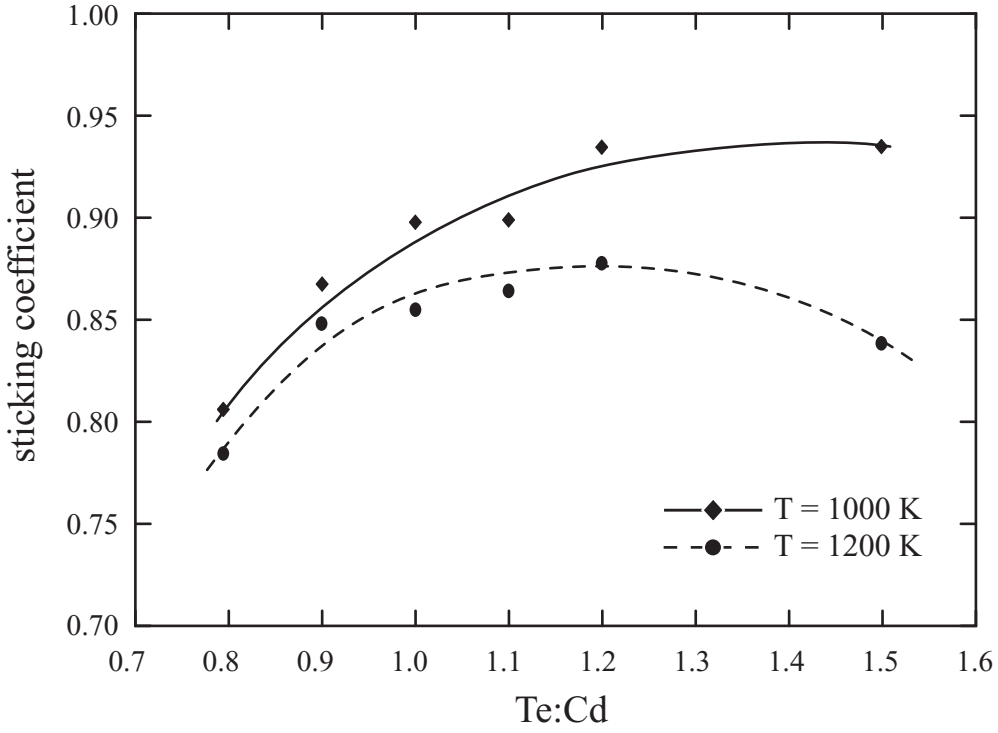
1.00
0.95
0.90
0.85
0.80
0.75
0.70
sticking coefficient
0.7
0.8
0.9
1.0
1.1
1.2
1.3
1.4
1.5
1.6
Te:Cd
T = 1000 K
T = 1200 K

Figure